

Numerical Study of Graphene Superlattice-Based Photodetectors

Mahdi Moradinasab, Mahdi Pourfath, *Member, IEEE*, Morteza Fathipour, *Member, IEEE*,
and Hans Kosina, *Member, IEEE*

Abstract—The optical properties of 1-D superlattices formed by armchair graphene nanoribbons embedded in hexagonal boron nitride superlattices (BNSLs) are studied. A set of tight-binding (TB) parameters is proposed, which gives results in excellent agreement with first-principle calculations. Based on the tight-binding model, it is demonstrated that in BNSLs, a larger bandgap opening is achieved than in hydrogen-passivated superlattices (HSL). The optical properties of BNSL and HSL are studied by employing the nonequilibrium Green function method and are verified with first-principle calculations. The role of line-edge roughness on the optical properties of such devices is carefully investigated.

Index Terms—Graphene superlattice, line-edge roughness, nonequilibrium Green's function (NEGF), optical properties, photodetector.

I. INTRODUCTION

THE controllable alteration of graphene by high-precision lithography [1]–[3] and chemical functionalization [4] has enabled modulation of the electronic, optical, and thermal properties of these structures. Graphene-based structures such as graphene nanoribbons (GNRs) [5], nanorods [6] quantum dots [7], and p-n junctions [8] have been successfully fabricated. A recent experimental study has reported ultra-smooth patterning of GNRs with modulated widths, which can be regarded as finite segments of GNR-based superlattices [3]. Such structures can behave as multiple quantum wells and exhibit interesting quantum effects [9], such as resonant tunneling [10]. Due to the possible application in nanoelectronics [11], photonics [12], and spintronics [13], an enormous volume of scientific work is being carried out on graphene-based structures.

Single-layer hexagonal boron nitride (h-BN) and boron nitride nanoribbons (BNNRs) that are regarded as the III-V

analogs of graphene and GNRs, respectively, have been synthesized and studied in recent years [14]–[16]. Theoretical and experimental results have shown that the sp^2 bonding in the BN lattice gains an ionic character due to different electronegativities of B and N, which causes the optical and electronic properties of BN and BNNRs to be substantially different from those of graphene and GNRs. Unlike graphene, which is a zero-gap material, h-BN has a wide bandgap of approximately 5.9 eV and shows a good insulating behavior [17].

The similarity of the crystal structures of BN and graphene gives rise to thermodynamically stable 2-D structures containing isolated regions of graphene and BN [18], [19]. These hybrid carbon-boron nitride (C-BN) structures can be synthesized by the approaches, such as thermal catalytic CVD methods [18]. Due to the relatively large ionicities of boron and nitride, BN-confined armchair graphene nanoribbons (AGNRs) exhibit a generally larger bandgap compared with H-passivated AGNRs [20], [21].

The first application of graphene as a photodetector has been demonstrated in [22]. A detectable current has been reported that is attributed to the band bending at the metal/graphene interface [23]. Photocurrents have also been obtained at single/bilayer graphene interfaces [24] and graphene p-n junctions [25]. More recent studies concentrate on increasing the photoresponsivity of the graphene devices [26] and extending their operation range to longer wavelengths [27].

In this paper, the optical properties of AGNR superlattice structures embedded in BN are investigated. The results indicate high responsivity and quantum efficiency, as well as long-wavelength operation, which render these devices as potential candidates for future photodetection applications.

The models for electronic bandstructure, transport of carriers, and electron–photon interactions are described in Section II. Simulation results are presented and discussed in Section III, and the conclusion is presented in Section IV.

II. APPROACH

Fig. 1 shows the structure of the studied superlattices. In the structure shown in Fig. 1(a), the dangling bonds of edge carbon atoms are saturated by hydrogen atoms, whereas in the structure shown in Fig. 1(b), the semiconducting region (formed by carbon atoms) is surrounded by BN. Throughout this paper, the structures in Fig. 1(a) and (b) are used as main structures that are referred to as HSL(11) and BNSL(11), respectively. The numbers inside the parentheses represent the number

Manuscript received November 26, 2012; revised December 7, 2014; accepted December 15, 2014. Date of current version January 20, 2015. This work was supported in part by the European Community's within the Seventh Framework Programme under Grant FP7-263306 and in part by the Austrian Science Fund under Grant F2514. The review of this paper was arranged by Editor J. Huang.

M. Moradinasab and M. Pourfath are with the School of Electrical and Computer Engineering, University of Tehran, Tehran 14395-515, Iran, and also with the Institute for Microelectronics, Technische Universität Wien, Wien 1040, Austria (e-mail: moradinasab@iue.tuwien.ac.at; pourfath@iue.tuwien.ac.at).

M. Fathipour is with the School of Electrical and Computer Engineering, University of Tehran, Tehran 14395-515, Iran (e-mail: mfathi@ut.ac.ir).

H. Kosina is with the Institute for Microelectronics, Technische Universität Wien, Wien 1040, Austria (e-mail: kosina@iue.tuwien.ac.at).

Color versions of one or more of the figures in this paper are available online at <http://ieeexplore.ieee.org>.

Digital Object Identifier 10.1109/TED.2014.2383354

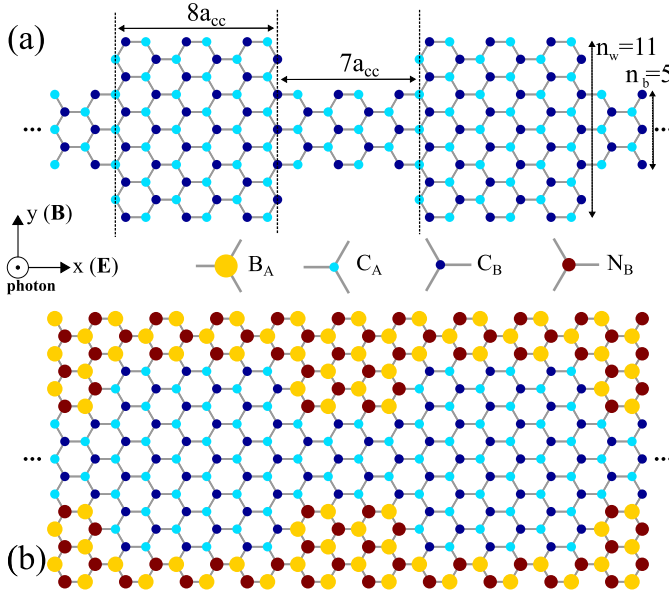


Fig. 1. Structures of (a) HSL and (b) boron nitride-confined superlattice. Both superlattices have the same index for the graphene nanoribbon part. $C_{A/B}$ represents a carbon, $N_{A/B}$ a nitride, and $B_{A/B}$ a boron atom at the sublattice A or B . n_w and n_b denote the well and barrier indices, respectively.

of carbon atoms along the width of the wider part of the superlattice (n_w). Lengths of $8a_{cc}$ and $7a_{cc}$ are considered for the well and barrier regions, respectively, where $a_{cc} = 1.42 \text{ \AA}$ is the carbon–carbon bonding distance. To investigate the optical properties of these superlattice structures, the nonequilibrium Green function (NEGF) formalism along with a TB model for the electronic bandstructure are employed.

A. First-Principle Calculations

For first-principle calculations, we employed the Spanish Initiative for Electronic Simulations with Thousands of Atoms package [28] with the following parameters: double- ζ basis set with additional orbitals of polarization for total energies and electronic bandstructures, the generalized gradient approximation method, Perdew–Burke–Ernzerhof as the exchange–correlation function, and the Troullier–Martins scheme for the norm-conserving pseudopotential calculations [20]. A grid cutoff of 210 Ry is chosen and the Brillouin zone sampling is performed by the Monkhorst–pack method. A mesh of $(128 \times 8 \times 1)$ has been adopted for discretization of the k -space. A broadening factor of 0.1 eV is assumed for the calculation of the joint density of states, and the convergence criterion for the density matrix is taken as 10^{-4} .

B. Tight-Binding Model

In graphene, three σ bonds hybridize in an sp^2 configuration, whereas $2p_z$ orbitals, which are perpendicular to the graphene layer, form π covalent bonds. We use a TB Hamiltonian of the π band electron to describe the electronic properties as

$$\hat{H} = t \sum_{\langle i,j \rangle} \hat{a}_i^\dagger \hat{a}_j. \quad (1)$$

The notation $\langle i,j \rangle$ represents a summation restricted between the pairs of the nearest-neighbor carbon/boron/nitride atoms, and t is the hopping parameter, which is described in the next section.

C. Line-Edge Roughness

Line-edge roughness plays an important role on the characteristics of narrow GNRs. Experimental data show that line-edge roughness is the dominant scattering mechanism for GNRs narrower than 60 nm [29]. Line-edge roughness causes fluctuations in the edge potential and leads to the modulation of the energy gaps, which affects optical transitions and photon absorption energies. Therefore, a careful investigation of this effect on the optical properties of GNR superlattices is essential. Line-edge roughness is a statistical phenomenon that can be well described by means of an exponential autocorrelation function [30]

$$R(x) = \Delta W^2 \exp\left(-\frac{|x|}{\Delta L}\right) \quad (2)$$

where ΔL is the roughness correlation length, which is a measure of smoothness, and ΔW is the root mean square of the fluctuation amplitude. To create line-edge roughness in real space, a random phase is added to the Fourier transform of the autocorrelation function (power spectrum) followed by an inverse Fourier transform [31]. Using the obtained roughness profiles, various devices are generated. The optical characteristics of each device are evaluated separately, followed by an ensemble average.

D. Nonequilibrium Green's Function

Over the past decade, the NEGF formalism has been widely employed to investigate various nanoelectronic devices [32]. Four types of the Green functions are defined as the nonequilibrium statistical ensemble averages of the single particle correlation operator. The greater Green function $G^>$ and the lesser Green function $G^<$ deal with the statistics of carriers. The retarded Green function G^R and the advanced Green function G^A describe the dynamics of carriers. Under steady-state condition, the equation of motion for the Green functions can be written as [32]

$$G^R(E) = [(E + i0^+)I - H - \Sigma(E)^R]^{-1} \quad (3)$$

$$G^{\lessgtr}(E) = G^R(E)\Sigma(E)\lessgtr G^A(E) \quad (4)$$

where H is the Hamiltonian matrix. In this formalism, the effect of various interactions is included in the self-energy term

$$\Sigma^R = \Sigma_1^R + \Sigma_2^R + \Sigma_s^R \quad (5)$$

where Σ_1 and Σ_2 are the self-energies of the left/right contacts and Σ_s is the scattering self-energy, respectively. The self-energy due to electron–photon interaction is considered in this paper. The Hamiltonian of the electron–photon interaction can be written as [33], [34]

$$\hat{H}_{e-ph} = \sum_{\langle i,j \rangle} \frac{q}{m_0} \hat{\mathbf{A}} \cdot \langle i|\hat{\mathbf{p}}|j \rangle \quad (6)$$

where $\hat{\mathbf{p}}$ is the momentum operator and $\hat{\mathbf{A}}$ is the vector potential. The second quantized vector potential $\hat{\mathbf{A}}$ is given by

$$\hat{\mathbf{A}} = \hat{\mathbf{a}} \sqrt{\frac{\hbar I_\omega}{2N_\omega \omega \epsilon c}} (\hat{b} e^{-i\omega t} + \hat{b}^\dagger e^{+i\omega t}). \quad (7)$$

The direction of $\hat{\mathbf{A}}$ is determined by the polarization of the field, which is denoted by $\hat{\mathbf{a}}$. Using the operator relation $\hat{\mathbf{p}} = (im_0/\hbar)[\hat{H}, \hat{\mathbf{r}}]$, one can rewrite the electron-photon interaction Hamiltonian as

$$\hat{H}_{e-ph} = \sum_{(l,m)} M_{l,m} (\hat{b} e^{-i\omega t} + \hat{b}^\dagger e^{+i\omega t}) \hat{a}_l^\dagger \hat{a}_m \quad (8)$$

$$M_{l,m} = (x_m - x_l) \frac{ie}{\hbar} \left(\frac{\hbar \sqrt{\epsilon_r \mu_r}}{2N_\omega \omega \epsilon c} I_\omega \right)^{1/2} \langle l | \hat{H}_0 | m \rangle \quad (9)$$

where x_m denotes the position of the carbon atom at site m and N_ω is the photon population number with the frequency ω . To evaluate (9), the commutator relation between Hamiltonian and position operator is used. In this relation, the matrix elements of the momentum can be calculated from $p_{x_{l,m}} = \langle l | \hat{p}_x | m \rangle$. As atomic orbitals in TB are unknown, it is common to use the gradient approximation [35] where the following commutator relation is used: $\hat{\mathbf{p}} = (im_0/\hbar)[\hat{H}, \hat{\mathbf{r}}]$. Therefore, the equation $p_{x_{l,m}} = \langle l | \hat{p}_x | m \rangle$ is given by

$$p_{x_{l,m}} = (im_0/\hbar) \langle l | Hx - xH | m \rangle. \quad (10)$$

The momentum matrix elements are, therefore, given by [36]

$$p_{x_{l,m}} = (x_m - x_l) \frac{im_0}{\hbar} \langle l | H | m \rangle. \quad (11)$$

The *photon flux* (I_ω) is defined as the number of photons per unit time per unit area [33], [37]

$$I_\omega \equiv P_{op}/(\hbar\omega) \quad (12)$$

where P_{op} is the incident power per unit area. The incident light is assumed to be monochromatic with a power of $P_{op} = 100 \text{ kW/cm}^2$ and polarized along the longitudinal axis (Fig. 1).

We employed the lowest order self-energy of the electron-photon interaction based on the self-consistent Born approximation [38]

$$\begin{aligned} \Sigma_{l,m}^<(E) = & \sum_{p,q} M_{l,p} M_{q,m} \\ & \times [N_\omega G_{p,q}^<(E - \hbar\omega) + (N_\omega + 1) G_{p,q}^<(E + \hbar\omega)] \end{aligned} \quad (13)$$

where the first term corresponds to the excitation of an electron by the absorption of a photon and the second term corresponds to the emission of a photon by de-excitation of an electron.

In this paper, a small voltage bias in the range of 0.05–0.1 V is applied to drive the generated electrons and holes toward the contacts. The restriction for the applied voltage bias is the band-to-band tunneling that increases the dark current and is detrimental for photodetectors. The tunneling current has an exponential dependence on the electric field. Due to the relatively small length of proposed

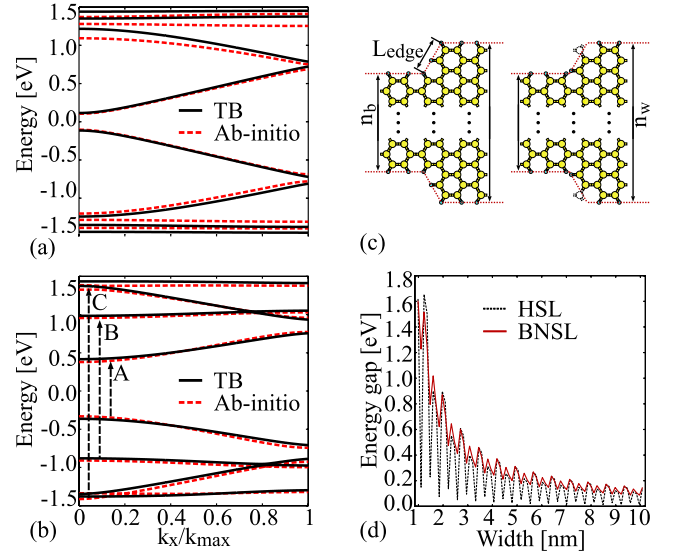


Fig. 2. Electronic bandstructures for (a) HSL(11) and (b) BNSL(11) based on the TB model and first-principles calculations. (c) Geometrical parameters of the structure. (d) Energy gap as a function of n_w for a HSL and a BNSL.

TABLE I

PROPOSED TB MODEL PARAMETERS FOR THE SUPERLATTICE. ALL PARAMETERS ARE EXPRESSED IN ELECTRON VOLTS

t_{CC}	t_{BB}	t_{NN}	t_{BC}	t_{NC}	t_{BN}
2.35	0	0.45	2.1	2.4	2.8
$t_{CC,2}$	$t_{BC,2}$	$t_{NC,2}$	Δ_{CC}	Δ_{BB}	Δ_{NN}
0	0.1	0.3	0.015	2.05	-2.05

superlattice photodetectors, applying even a small voltage bias may cause a huge electric field. For example, a voltage bias of 0.1 V leads to an electric field of $4.7 \times 10^5 \text{ V/cm}$.

III. RESULTS AND DISCUSSION

Fig. 2 compares the bandstructures for HSL(11) and BNSL(11) based on the TB model and first principles calculations. Carbon-carbon interactions up to three nearest neighbors are considered in the TB calculations for HSLs. In the case of BNSLs, a more careful choice of the TB parameters is required due to the ionicities of the boron and nitride atoms at the edges of the superlattice.

The TB parameters proposed in Table I result in electronic disperse relations that are in excellent agreement with first-principle simulations. In this table, t_{XY} and $t_{XY,2}$ denote the hopping parameter between the first and second nearest neighbor X and Y atoms, where X and Y represent carbon C , boron B , or nitride N atoms. Δ_{XX} denotes the on-site potential of atom X . As shown in Fig. 2(a), larger energy gaps are achieved for BNSLs in comparison with HSLs, which is attributed to the large ionic potential difference between boron and nitride atoms in BNSLs [20].

The bandgap as a function of the width of superlattice is shown in Fig. 2(d). Zigzag edges in a graphene layer induce an opposite spin orientation across the ribbon between ferromagnetically ordered edge state [39]. In such cases, additional spin analysis is necessary, which is beyond the scope of this

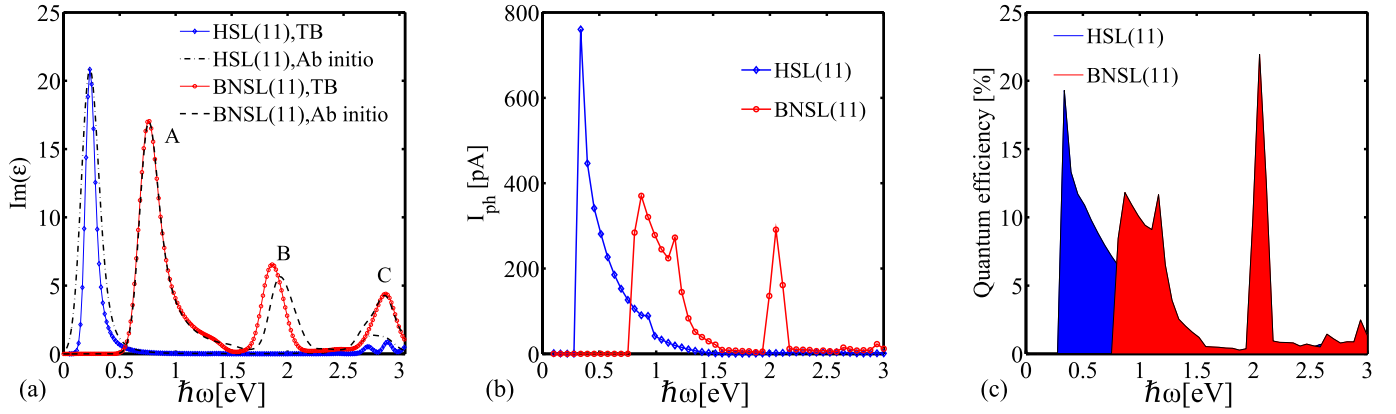


Fig. 3. (a) Dielectric response of a HSL(11) and a BNSL(11) based on the TB (solid lines) and first-principle calculations (dashed lines). (b) Photocurrent and (c) quantum efficiency for a HSL(11) and a BNSL(11). The optical power density is 100 kW/cm^2 and the photon flux is assumed to be normal to the HSL/BNSL plane.

paper. To avoid zigzag edges, we assumed that n_w and n_b are scaled such that L_{edge} is kept constant, where n_w and n_b are defined as the number of dimer lines in the well and barrier of the superlattice, respectively [Fig. 2(c)]. Fig. 2(d) shows that HSLs, unlike BNSLs, have relatively small bandgap for specific values of $n_w = 3p + 2$, where p is a positive integer. In addition, the scaling of the energy gap with the width in BNSLs shows a more uniform behavior compared with that of HSLs. An important point to notice is the instability of the superlattice shown in the right side of Fig. 2(c) as a result of the dangling bonds, which will quickly relax to form another geometry. In fact, all superlattices with even values of n_w are unphysical, and thus, the studies are restricted to odd values of n_w .

The optical response of the superlattices presented in Fig. 1 is studied in terms of the interband dielectric response function. In the linear response regime, the imaginary part of the interband dielectric response function at a given frequency is given by [40]

$$\epsilon_i(\omega) = \frac{1}{4\pi\epsilon_0} \left(\frac{2\pi e}{m\omega} \right)^2 \sum_{k_x} |p_{c,v}|^2 \delta(E_c(k_x) - E_v(k_x) - \hbar\omega) \times [f(E_v(k_x)) - f(E_c(k_x))] \quad (14)$$

where $\hbar\omega$ is the energy of the incident photons. The Dirac delta function $\delta(E)$ is approximated by a Gaussian function with a broadening factor of 0.1 eV. The real part of the dielectric function $\epsilon_r(\omega)$ is evaluated from the imaginary part using the Kramers–Kronig relation [40]. The optical conductivity is related to the dielectric function by $\epsilon(\omega) = 1 + 4\pi i \sigma(\omega)/\omega$ [40].

Fig. 3(a) compares the imaginary parts of the dielectric functions for a HSL(11) and a BNSL(11). The absorption spectrum exhibits its first peak at $\hbar\omega = 0.33 \text{ eV}$, which corresponds to a transition from the highest valence band to the lowest conduction band. The optical absorption spectrum of BNSL(11) exhibits additional peaks in the photon energy range $0 < \hbar\omega < 3.5 \text{ eV}$. The absorption peaks occur at the photon energies of 0.91, 1.965, and 3.156 eV, which are related to transitions represented by A, B, and C in Fig. 2(b), respectively. The comparison of

the dielectric functions in Fig. 3(a) with the bandstructures shown in Fig. 2(a) and (b) suggests that for this specific structure, only the transitions from valence bands to conduction bands with the same index are allowed. This, however, is not a general transition rule for BNSLs and does not hold at various geometrical parameters.

To assess the performance of superlattice structures for photodetection applications, the quantum efficiency and the photoresponsivity of the presented structures are evaluated. The quantum efficiency is defined as $\alpha = (I_{ph}/q)/(P_{op}/\hbar\omega)$, where I_{ph} and P_{op} are the photocurrent and the incident optical power, respectively. Fig. 3(b) and (c) shows the calculated photocurrent and quantum efficiency as a function of the incident photon energy, respectively, for HSL(11) and BNSL(11). The quantum efficiency peaks if the photon energy corresponds to an allowed intersubband optical transition. The quantum efficiency of the HSL reaches the values of about 20%, which is significantly larger than that of H-passivated AGNRs [41]. For the case of BNSL(11), there are more peaks in the specified energy range due to the different subband spacings in comparison with those of HSL(11). Quantum efficiencies of 13% and larger than 20% are obtained for the first and second peaks in the optical spectrum, respectively. The photoresponsivities—defined as I_{ph}/P_{op} —of HSL and BNSL reach 0.866 A/W and 0.303 A/W, respectively, where the optical power is assumed to be 100 kW/cm^2 .

The structural parameters effects on superlattice photodetector characteristics are examined. Fig. 4(a) and (b) indicates that more peaks appear in the quantum efficiencies of HSL/BNSL(13) and HSL/BNSL(17) compared with the main structure [Fig. 3(c)]. If the width of the superlattice increases, energy gaps decrease that allow more optical transitions. This behavior is similar to that of GNRs [30]; however, in superlattice photodetectors, the quantum efficiencies at higher energies are larger in comparison with that of lower energies. This is due to the presence of barriers that block transport of photogenerated carriers, which is more pronounced by increasing the barrier/well lengths [Fig. 4(c) and (d)]. It should be noted that the confinement due to the presence of barriers only weakly affects devices with relatively long wells and the characteristics

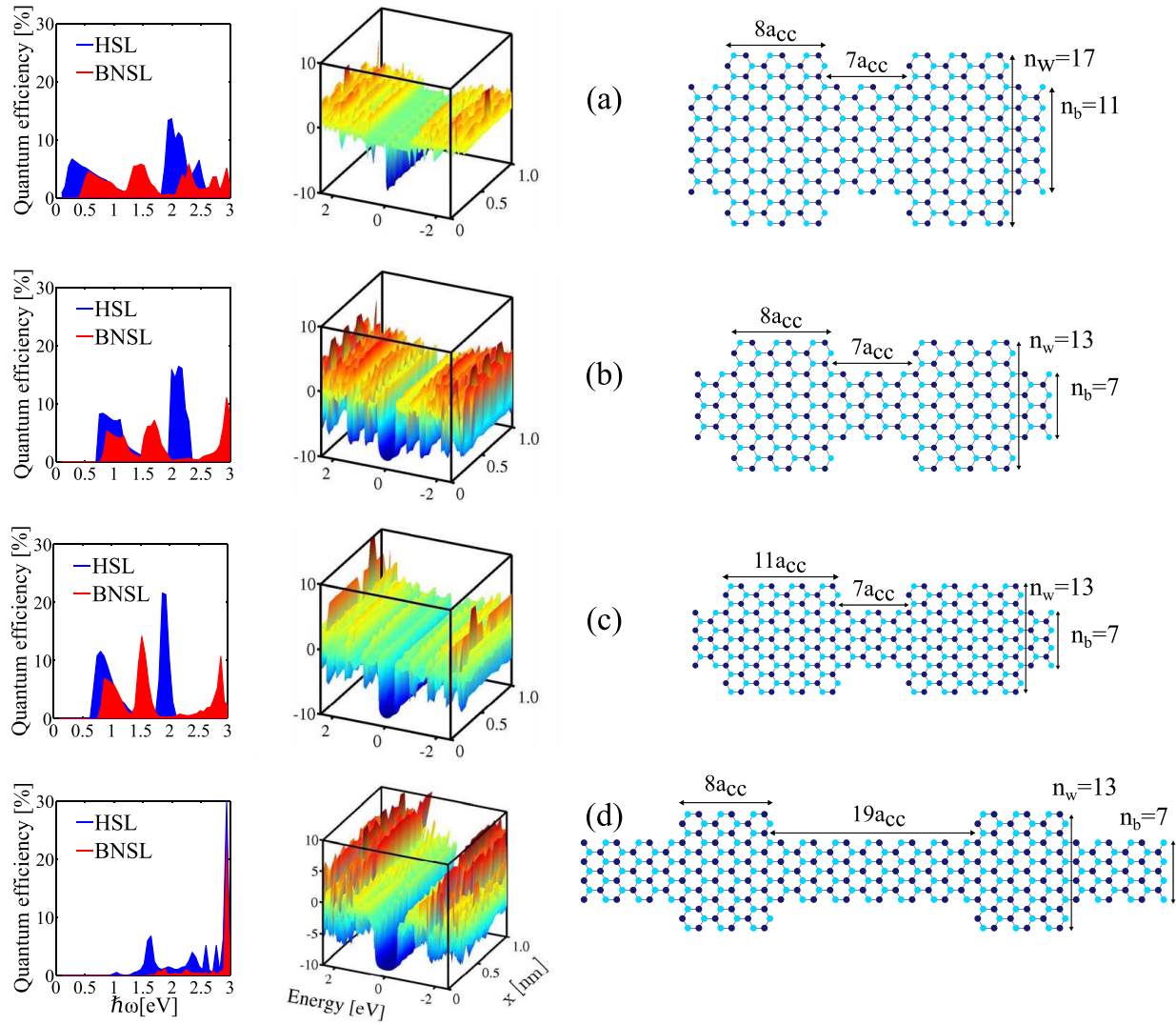


Fig. 4. Structures of (a) HSL(13) and (b) HSL(17). (c) and (d) Superlattices with different well/barrier lengths. The quantum efficiency and local density of states of each structure are depicted.

of such structures become similar to conventional GNR-photodetectors.

The effect of line-edge roughness on the electronic properties of GNRs has been investigated in several analytical [30], [42] and numerical studies [43], [44]. Here, we investigate the role of roughness on the spectrum of photocurrent in GNR-based superlattices. We add/remove an integer number of atoms from the edges based on their relative position with respect to the generated rough edge. However, this may result in unstable edge-structures with monomers instead of dimmers at the edges. In these cases, the edges are reconstructed to be physically stable [Fig. 5(e)–(g)]. For the given geometrical and roughness parameters, many samples are statistically generated. The characteristics of each device are evaluated followed by an ensemble average over all samples. More details about our approach can be found in [31].

Fig. 5 exhibits the results for HSL(11) and BNSL(11) with edge disorders. Roughness is expressed in terms of n_w because the well has a more significant effect on the optical transitions. The absolute roughness amplitude is

the same all over the device. In the case of BNSL(11), the roughness is applied at the C-BN interfaces. As it is shown in Fig. 1, a BN passivation with 2/3 dimmers is considered in BNSLs. For the roughness amplitudes of 3%, 4%, and 5%, the structures are still passivated with BN. However, for larger roughness amplitudes, the roughness may cross the boundaries without any BN passivation. In these cases, the structures are reconstructed by additional BN dimmers at the boundaries.

Due to backscattering of carriers, the photocurrent and quantum efficiencies of both superlattices decrease in the presence of line-edge roughness. Fig. 5(a) shows that due to effective width variation, the photoabsorption peaks appear at energies larger or smaller than the peaks of the structure without disorder. The average width of edge-defected devices, however, is equal to that of a device with perfect edges. Therefore, line-edge roughness does not affect the location of the average photocurrent peak.

HSL(11) exhibits photoresponsivity and quantum efficiency reductions of 23%, 55%, and 70% for the relative

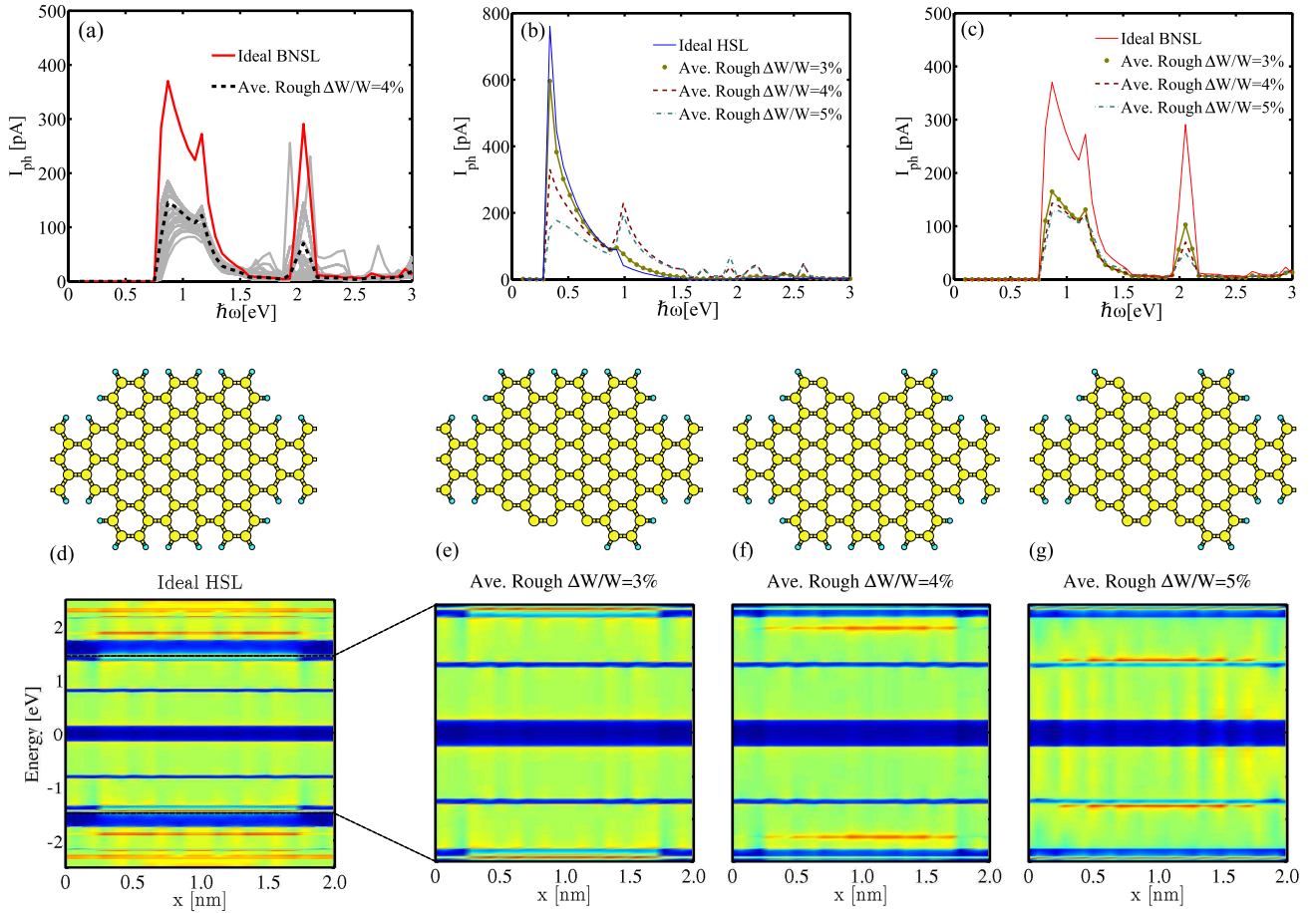


Fig. 5. (a) Average photocurrent spectrum over different samples (dashed-black line) and photocurrent spectrum of each sample as a function of the incident photon energy (gray lines). The ideal and average photocurrent spectra for (b) HSL(11) and (c) BNSL(11). Local density of states for (d) ideal and (e)–(g) rough HSL(11) at various roughness amplitudes. The optical power density is 100 kW/cm² and the photon flux is assumed to be normal to the HSL/BNSL plane.

roughness amplitudes of 3%, 4%, and 5%, respectively, whereas a smoother behavior is observed for BNSL(11) [comparing Fig. 5(b) and (c)]. This behavior is attributed to the stable configuration of edge-carbon atoms in BNSL in comparison with HSL in the presence of line-edge roughness. The average photocurrent of edge-defected HSLs peaks at photon energies around $\hbar\omega = 1$ eV. This peak is related to line-edge roughness induced states [Fig. 5(e)–(g)]. Due to the formation of dangling bonds in the presence of line-edge roughness, these states are formed. As the relative roughness amplitude increases, more states are induced and more photocurrent is generated by transitions from these states. However, dangling bonds are absent in edge-defected BNSLs and such states do not appear in such structures.

IV. CONCLUSION

In this paper, the optical properties of graphene nanoribbon superlattices embedded in boron nitride sheets and the possibility of using such structures as photodetectors are studied. We propose a set of TB parameters for the investigated structures, which shows an excellent agreement with first-principles results. The results indicate that the optical spectrum of a BN-confined AGNR superlattice contains more absorption peaks and show more optical intersubband

transitions compared with a hydrogen passivated superlattice with the same geometry. Employing the NEGF method, the photocurrents and quantum efficiencies are evaluated and compared for both devices at various incident photon energies.

Using an statistical approach, the role of line-edge roughness on the optical properties of GNR-based superlattices is investigated. The results indicate that the quantum efficiency and photoresponsivity decrease in the presence of line-edge roughness. For HSL, induced states appear and increase with the roughness amplitude, which result in the appearance of an additional peak in photocurrent spectrum. In comparison with HSLs, BNSL photodetectors exhibit more robust optical properties in the presence of line-edge roughness due to stable edge atom configuration.

REFERENCES

- [1] S.-C. Jeon, Y.-S. Kim, and D.-K. Lee, "Fabrication of a graphene nanoribbon with electron beam lithography using a XR-1541/PMMA lift-off process," *Trans. Elect. Electron. Mater.*, vol. 11, no. 4, pp. 190–193, 2010.
- [2] L. P. Biró and P. Lambin, "Nanopatterning of graphene with crystallographic orientation control," *Carbon*, vol. 48, no. 10, pp. 2677–2689, 2010.
- [3] X. Li, X. Wang, L. Zhang, S. Lee, and H. Dai, "Chemically derived, ultrasmooth graphene nanoribbon semiconductors," *Science*, vol. 319, no. 5867, pp. 1229–1232, 2008.

- [4] N. Gorjizadeh and Y. Kawazoe, "Chemical functionalization of graphene nanoribbons," *J. Nanomater.*, vol. 2010, pp. 513501-1–513501-7, Jan. 2010.
- [5] K. S. Novoselov *et al.*, "Two-dimensional gas of massless Dirac fermions in graphene," *Nature*, vol. 438, no. 7065, pp. 197–200, 2005.
- [6] G. Seol and J. Guo, "Assessment of graphene nanomesh and nanoroad transistors by chemical modification," in *Proc. IEEE Int. Electron Devices Meeting (IEDM)*, Dec. 2011, pp. 2.3.1–2.3.4.
- [7] Z. F. Wang *et al.*, "Chiral selective tunneling induced negative differential resistance in zigzag graphene nanoribbon: A theoretical study," *Appl. Phys. Lett.*, vol. 92, no. 13, pp. 133114-1–133114-3, Mar. 2008.
- [8] H.-C. Cheng, R.-J. Shiue, C.-C. Tsai, W.-H. Wang, and Y.-T. Chen, "High-quality graphene p - n junctions via resist-free fabrication and solution-based noncovalent functionalization," *ACS Nano*, vol. 5, no. 3, pp. 2051–2059, 2011.
- [9] H. Sevinçli, M. Topsakal, and S. Ciraci, "Superlattice structures of graphene-based armchair nanoribbons," *Phys. Rev. B*, vol. 78, no. 24, pp. 245402-1–245402-8, 2008.
- [10] H. Teong, K.-T. Lam, S. B. Khalid, and G. Liang, "Shape effects in graphene nanoribbon resonant tunneling diodes: A computational study," *J. Appl. Phys.*, vol. 105, no. 8, pp. 084317-1–084317-6, Apr. 2009.
- [11] M. Freitag, "Graphene: Nanoelectronics goes flat out," *Nature Nanotechnol.*, vol. 3, no. 8, pp. 455–457, 2008.
- [12] T. Mueller, F. Xia, and P. Avouris, "Graphene photodetectors for high-speed optical communications," *Nature Photon.*, vol. 4, no. 5, pp. 297–301, 2010.
- [13] S. Rakheja and A. Naemi, "Graphene nanoribbon spin interconnects for nonlocal spin-torque circuits: Comparison of performance and energy per bit with CMOS interconnects," *IEEE Trans. Electron Devices*, vol. 59, no. 1, pp. 51–59, Jan. 2012.
- [14] A. Nagashima, N. Tejima, Y. Gamou, T. Kawai, and C. Oshima, "Electronic structure of monolayer hexagonal boron nitride physisorbed on metal surfaces," *Phys. Rev. Lett.*, vol. 75, no. 21, pp. 3918-1–3918-4, 1995.
- [15] T. O. Wehling *et al.*, "Molecular doping of graphene," *Nano Lett.*, vol. 8, no. 1, pp. 173–177, 2008.
- [16] F. Zheng, K.-I. Sasaki, R. Saito, W. Duan, and B.-L. Gu, "Edge states of zigzag boron nitride nanoribbons," *J. Phys. Soc. Jpn.*, vol. 78, no. 7, pp. 074713-1–074713-6, 2009.
- [17] X. Gao, Z. Zhou, Y. Zhao, S. Nagase, S. B. Zhang, and Z. Chen, "Comparative study of carbon and BN nanographenes: Ground electronic states and energy gap engineering," *J. Phys. Chem. C*, vol. 112, no. 33, pp. 12677-1–12677-6, 2008.
- [18] L. Ci *et al.*, "Atomic layers of hybridized boron nitride and graphene domains," *Nature Mater.*, vol. 9, no. 5, pp. 430–435, 2010.
- [19] Y. Ding, Y. Wang, and J. Ni, "Electronic properties of graphene nanoribbons embedded in boron nitride sheets," *Appl. Phys. Lett.*, vol. 95, no. 12, pp. 123105-1–123105-3, 2009.
- [20] G. Seol and J. Guo, "Bandgap opening in boron nitride confined armchair graphene nanoribbon," *Appl. Phys. Lett.*, vol. 98, no. 14, pp. 143107-1–143107-3, Apr. 2011.
- [21] H. Nematian, M. Moradinasab, M. Pourfath, M. Fathipour, and H. Kosina, "Optical properties of armchair graphene nanoribbons embedded in hexagonal boron nitride lattices," *J. Appl. Phys.*, vol. 111, no. 9, pp. 093512-1–093512-6, May 2012.
- [22] E. J. H. Lee, K. Balasubramanian, R. T. Weitz, M. Burghard, and K. Kern, "Contact and edge effects in graphene devices," *Nature Nanotechnol.*, vol. 3, no. 8, pp. 486–490, 2008.
- [23] A. Pospischil *et al.*, "CMOS-compatible graphene photodetector covering all optical communication bands," *Nature Photon.*, vol. 7, no. 11, pp. 892–896, 2013.
- [24] X. Xu, N. M. Gabor, J. S. Alden, A. M. van der Zande, and P. L. McEuen, "Photo-thermoelectric effect at a graphene interface junction," *Nano Lett.*, vol. 10, no. 2, pp. 562–566, 2010.
- [25] M. C. Lemme *et al.*, "Gate-activated photoresponse in a graphene p - n junction," *Nano Lett.*, vol. 11, no. 10, pp. 4134–4137, 2010.
- [26] G. Konstantatos *et al.*, "Hybrid graphene–quantum dot phototransistors with ultrahigh gain," *Nature Nanotechnol.*, vol. 7, no. 6, pp. 363–368, 2012.
- [27] J. Yan *et al.*, "Dual-gated bilayer graphene hot-electron bolometer," *Nature Nanotechnol.*, vol. 7, no. 7, pp. 472–478, 2012.
- [28] J. M. Soler *et al.*, "The SIESTA method for *ab initio* order- N materials simulation," *J. Phys., Condens. Matter*, vol. 14, no. 11, pp. 2745–2779, 2002.
- [29] Y. Yang and R. Murali, "Impact of size effect on graphene nanoribbon transport," *IEEE Electron Device Lett.*, vol. 31, no. 3, pp. 237–239, Mar. 2010.
- [30] A. Y. Goharrizi, M. Pourfath, M. Fathipour, H. Kosina, and S. Selberherr, "An analytical model for line-edge roughness limited mobility of graphene nanoribbons," *IEEE Trans. Electron Devices*, vol. 58, no. 11, pp. 3725–3735, Nov. 2011.
- [31] A. Yazdanpanah, M. Pourfath, M. Fathipour, H. Kosina, and S. Selberherr, "A numerical study of line-edge roughness scattering in graphene nanoribbons," *IEEE Trans. Electron Devices*, vol. 59, no. 2, pp. 433–440, Feb. 2012.
- [32] M. Pourfath, *The Non-Equilibrium Green's Function Method for Nanoscale Device Simulation*. Vienna, Austria: Springer-Verlag, 2014.
- [33] L. E. Henrickson, "Nonequilibrium photocurrent modeling in resonant tunneling photodetectors," *J. Appl. Phys.*, vol. 91, no. 10, pp. 6273–6281, May 2002.
- [34] D. A. Stewart and F. Léonard, "Photocurrents in nanotube junctions," *Phys. Rev. Lett.*, vol. 93, no. 10, p. 107401, 2004.
- [35] G. Dresselhaus and M. S. Dresselhaus, "Fourier expansion for the electronic energy bands in silicon and germanium," *Phys. Rev.*, vol. 160, no. 3, pp. 649–679, 1967.
- [36] T. G. Pedersen, K. Pedersen, and T. B. Kriestensen, "Optical matrix elements in tight-binding calculations," *Phys. Rev. B*, vol. 63, pp. 201101(R)-1–201101(R)-4, May 2001.
- [37] U. Aeberhard and R. H. Morf, "Microscopic nonequilibrium theory of quantum well solar cells," *Phys. Rev. B*, vol. 77, pp. 125343-1–125343-9, Mar. 2008.
- [38] R. Lake, G. Klimeck, R. C. Bowen, and D. Jovanovic, "Single and multiband modeling of quantum electron transport through layered semiconductor devices," *J. Appl. Phys.*, vol. 81, no. 12, pp. 7845–7869, 1997.
- [39] Y.-W. Son, M. L. Cohen, and S. G. Louie, "Half-metallic graphene nanoribbons," *Nature*, vol. 444, no. 7117, pp. 347–349, 2006.
- [40] P. Y. Yu and M. Cardona, *Fundamentals of Semiconductors: Physics and Materials Properties*. Berlin, Germany: Springer-Verlag, 2001.
- [41] M. Pourfath, O. Baumgartner, H. Kosina, and S. Selberherr, "Performance evaluation of graphene nanoribbon infrared photodetectors," in *Proc. 9th Int. Conf. Numer. Simulation Optoelectron. Devices*, Gwangju, Korea, Sep. 2009, pp. 13–14.
- [42] D. Gunlycke and C. T. White, "Scaling of the localization length in armchair-edge graphene nanoribbons," *Phys. Rev. B*, vol. 81, pp. 075434-1–075434-6, Feb. 2010.
- [43] S. M.-M. Dubois *et al.*, "Quantum transport in graphene nanoribbons: Effects of edge reconstruction and chemical reactivity," *ACS Nano*, vol. 4, no. 4, pp. 1971–1976, 2010.
- [44] A. Y. Goharrizi, M. Pourfath, M. Fathipour, and H. Kosina, "Device performance of graphene nanoribbon field-effect transistors in the presence of line-edge roughness," *IEEE Trans. Electron Devices*, vol. 59, no. 12, pp. 3527–3532, Dec. 2012.



Mahdi Moradinasab received the M.S. degree in electrical engineering from the University of Tehran, Tehran, Iran, in 2009. He is currently pursuing the Ph.D. degree in technical sciences with the Technische Universität Wien, Vienna, Austria.

His current research interests include numerical study of novel semiconductor devices, quantum transport in nanostructures, optical properties of nanostructures, and photonics.



Mahdi Pourfath (M'08) received the Ph.D. degree from the Technische Universität Wien, Vienna, Austria, in 2007.

He has been with the Technische Universität Wien since 2008. He is also currently with the University of Tehran, Tehran, Iran.



Morteza Fathipour (M'90) received the Ph.D. degree from Colorado State University, Fort Collins, CO, USA, in 1984.

He is currently with the University of Tehran, Tehran, Iran.



Hans Kosina (S'89–M'93) received the Ph.D. degree from the Technische Universität Wien, Vienna, Austria, in 1992.

He is currently an Associate Professor with the Institute for Microelectronics, Technische Universität Wien.